Metrologia 12, 169–179 (1976)

Metrologia

Spectrometry of a ^{60}Co Gamma-Ray Beam Used for Instrument Calibration

M. Ehrlich and S. M. Seltzer
Center for Radiation Research, National Bureau of Standards, Washington, D.C. 20234, USA
M. J. Bielefeld
Computer Sciences Corporation, Silver Spring, MD 20910, USA
J. I. Trombka
Goddard Space Flight Center, Greenbelt, MD 20771, USA

Received: March 17, 1976

Abstract

Measurements were made of the spectrum of one of the collimated ^{60}Co gamma-ray beams employed in the instrument-calibration program of the National Bureau of Standards. The high-activity calibration-source capsule was replaced by one of low activity and identical geometry. The contributions to the spectrum by the scatter from the low-activity replacement source, the housing, and the collimation system were isolated by means of supplementary measurements in free air carried out on the replacement source and on a scatter-free source. Depending on collimator setting, the scatter contribution below 1 MeV was found to be between 13 and 19 percent of the total number of photons in the beam. A description is given of the measurements and of the technique for data reduction. Detailed spectral results are presented.

1. Introduction

As a part of a long-range program of providing adequate characterization of the x- and gamma-ray beams employed in the instrument-calibration program of the National Bureau of Standards (NBS), measurements were made of the spectrum emerging from the collimated ^{60}Co gamma-ray facility, including the contribution of scattered photons down to about 0.05 MeV. For this purpose, the high-activity calibration source was replaced by a low-activity source of identical configuration. By measuring the spectrum of this source both inside and outside the collimated housing, and comparing it with the spectrum of an essentially scatter-free reference source, the scattered radiation due to the various components of the facility could be identified.

Spectra emerging from commonly used ^{60}Co gamma-irradiation facilities have been obtained on several occasions from pulse-height distributions arising in NaI(Tl) scintillation spectrometers, either by means of simulation through low-activity sources [1, 2] or through measurements in the once-scattered beams [3, 4]. A summary of past results up to 1970 is given in ICRU Report 18 [5]. In spite of the availability of the results of other investigators, it is often necessary to carry out independent measurements because of the unique features of a particular irradiation facility. One of the more recent studies of this nature is that of Guiho *et al.* [6] who measured the spectra emerging from two different housings loaded with ^{60}Co disc-and pellet-type sources in a number of different geometries. They indicate that they used a computerized least-squares data-reduction technique for arriving at the spectral distributions of the photon beams, but give no further details nor references to it.

For the results discussed in the present paper, a data-reduction technique developed at the Goddard Space Flight Center, National Aeronautics and Space Administration, was employed [7–9]. A description is given of the experimental setup, the measurement techniques, and the methods used in data reduction, including an assessment of uncertainties. Results are presented for the scatter contributions of the source in its capsule, the housing, and the collimation system, and are compared with those obtained by other authors for different source and housing geometries.

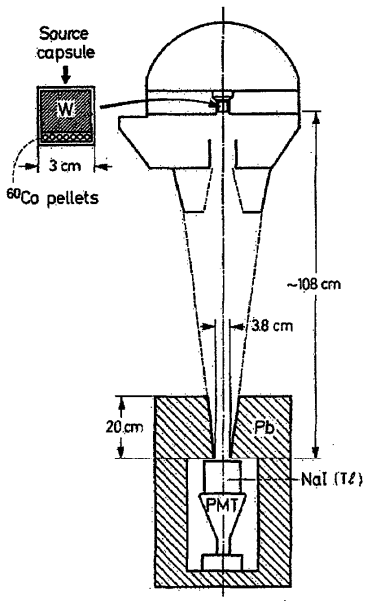

Fig. 1. Experimental setup. The source-capsule insert shows the activated ^{60}Co pellets backed by a tungsten plug; the capsule is of stainless steel

2. Experimental Setup

Source Geometry

The vertical-beam ^{60}Co gamma-ray facility used at NBS for radiation-instrument calibration is shown schematically in Fig. 1, along with the detector assembly used in these measurements. It consists of an "Eldorado Super G" unit of the Atomic Energy of Canada, Ltd. (AECL), equipped with the AECL G754 variable collimator.* This unit is similar to (but not identical with) the unit employed in the studies of Aitken and Henry [2]. The sources customarily supplied by AECL with this and other types of units consist of nickel-plated cylindrical ^{60}Co pellets, of a height and diameter of about 1 mm, contained in a steel cylinder and backed by a steel plug. Aitken and Henry [2] and also Guiho et al. [6] in their comparative studies of source geometries used this type of source, varying the inner diameter of the steel cylinder between 10 and 25 mm, and the depth of the source-pellet layer between 7 and 25 mm. The NBS calibration source, which at the time of these measurements had an activity of around 20 TBq (500 Ci), was supplied by AECL to NBS specifications. It consists of a steel cylinder of an inner diameter of 30 mm and essentially one single layer of pellets, backed by a tungsten plug. The single-layer source geometry was chosen to keep absorption and degradation of the gamma radiation in the source proper at a low level, and the high-Z plug to keep the back-scatter contribution low. For the present spectral measurements, this source was replaced by a source of identical geometry, but with an activity of about 15 MBq (400 μ Ci). This source is referred to as the "simulation source."

Choice of Detector

The choice of a detector suitable for ^{60}Co gamma-ray spectrometry is difficult. Of interest is the spectrum of the scattered radiation produced by the primary ^{60}Co gamma radiation interacting with matter prior to reaching the detector. This spectrum is a continuum, spanning the energy range from 1.33 MeV down to about 100 keV. The task is to distinguish between this scatter continuum and the escape component of the detector response to the incident unscattered 1.17-MeV and 1.33-MeV gamma-ray photons. Desirable detector characteristics for accomplishing this task are (a) a small escape component (high total-absorption efficiency), and (b) good resolution, to prevent a masking of the scatter spectrum of interest by the dominant gamma-ray lines. Available germanium detectors have good resolution, but because of their relatively small size produce large ^{60}Co gamma-ray escape components. The resolution of NaI(Tl) scintillation detectors is poorer, but they may be obtained large enough for high absorption efficiency. For the present study, it was decided to use a large NaI(Tl) scintillation crystal in a trade-off of high resolution for high absorption efficiency, and to utilize sophisticated data-handling procedures in order to recover as much of the information content as possible.

The detector assembly shown in Figure 1 consisted of a 12.7-cm diameter, 10.2-cm thick NaI(Tl) crystal mounted on a magnetically shielded photomultiplier tube with a front face somewhat larger than the crystal diameter. The sealed aluminum can containing the detector-photomultiplier assembly was mounted in a lead-brick housing about 5 cm thick at the bottom and of 10 cm wall thickness. The lead layer facing the source was about 20 cm thick and had a central opening in the shape of a truncated cone, which served as a beam collimator. This collimator was large enough to allow the detector to see all the scattered radiation emerging from the source collimator, in addition to the primary photons. The lead housing was mounted on a steel platform that could be moved vertically to vary the distance of the detector from the stationary source between about 1 and 2 meters. While the smallest diameter of the collimator cone was kept constant, the largest diameter was adjusted according to source-to-detector distance so that all scattered photons emerging from the source collimator could reach the detector. The photomultiplier assembly was shielded against the K x rays produced in the lead of the detector housing by a liner of brass and aluminum on the sides, and by steel and aluminum on top of the inner cavity. A NBS-built preamplifier, a commercial multimode amplifier, and a commercial 400-channel pulse-height analyzer

* Commercial equipment is identified here in order to specify the experimental procedure uniquely. This identification does not imply a recommendation or endorsement by NBS nor does it imply that NBS considers the identified equipment to be the best available for the purpose.

coupled to a teletypewriter with tape punch completed the setup.

Spectral Measurements

With the simulation source inside the housing, spectra were obtained for two detector distances and a wide range of collimator settings. In order to be able to separate the scatter component measured for these spectra into the contribution of the source head and collimator, and the contribution of the simulation source proper, further measurements were made at the same two detector distances with the simulation source free in air, and with an additional essentially scatter-free source, in a room about 4½ m high, with a floor space of about 6 m x 9 m. The scatter-free source was one of a set of NBS Standard Reference Material point sources used for the calibration of the spectrometer. These sources are made by depositing a drop of a solution of a suitable compound of the radionuclide (e.g., cobalt in the form of its chloride) on polyester tape, approximately 6 μm thick, and covering it with another layer of the same tape.* The spectra were measured with the simulation source and the scatter-free source supported on polyester tape stretched across a plastic frame. The frame was placed at a fixed location in the room, so as to eliminate the influence of room and air scatter on the difference spectrum.

3. Data Reduction

The photon spectra are related to the measured pulse-height distributions through the convolution

$$H(h) = \int_0^\infty R(E, h)\, T(E)\, dE, \qquad (1)$$

where $R(E, h)$ is the detector response function, defined as the probability per unit energy that a photon incident on the detector with energy E gives rise to a pulse recorded with height h; $H(h)$ is the measured pulse-height distribution; and $T(E)$ is the photon spectrum of interest. In principle, it is possible to measure the response function of the detector in detail. However, the limited number of suitable monoenergetic gamma-ray sources and the complex structure of the function itself make it difficult to develop – solely on an experimental basis – a body of data with detail sufficient for the accurate interpolation necessary in the unfolding procedure. The method chosen here combines information from calibration experiments using scatter-free point sources of ^{22}Na, ^{60}Co, ^{137}Cs, and ^{109}Cd with that from theoretical computations. In the following, the construction of the response-function matrix and the solution of Eq. (1) is sketched briefly.

* Standard Reference Materials may be purchased through the Office of Standard Reference Materials, National Bureau of Standards, Washington, D.C. 20234, USA.

3.1. The Response Function

The component parts of the response function may be represented schematically as

$$R(E_0, h) = \eta(E_0) \int_0^{E_0} D(E_0, E) G(E, h)\, dE. \qquad (2)$$

In this equation, $\eta(E_0)$ is the detection efficiency (the probability that the incident gamma ray of energy E_0 will have at least one interaction in the detector); $D(E_0, E)$ is the energy deposition spectrum which gives rise to the well-known characteristics of the response function: the photopeak, the x-ray escape peak, and the continuous escape component; and $G(E, h)$ is the detector resolution function, which produces the typically Gaussian line shapes. Non-linearities in the photon-energy-to-pulse-height conversion usually are accounted for on the basis of information on the relationship between pulse height and photopeak location, obtained experimentally. (See Fig. 3.)

Energy-Deposition Spectrum and Detection Efficiency: A Monte-Carlo method described in detail elsewhere [10], was used to compute the energy-deposition spectrum, $D(E_0, E)$, for a bare NaI crystal of the dimensions used in this experiment. Results suitably scaled so as to facilitate interpolation [10] were obtained for thirteen photon energies, E_0, ranging from 0.05 to 1.50 MeV. The incident photons were assumed to be in the form of a plane-parallel beam with a diameter equal to that of the detector collimator used in the measurements. Possible contributions due to photons scattered by the detector collimator, detector canning material, and adjacent electronics, were not included. With this beam geometry the detection efficiency, $\eta(E_0)$, could be calculated analytically.

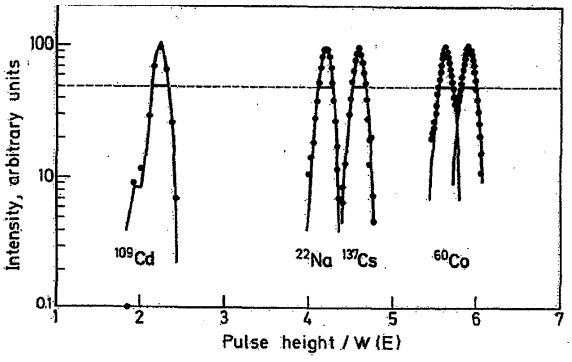

Fig. 2. Detector resolution. Points – experimental calibration data; solid lines – theoretical response-function peaks. Dashed line indicates one-half of peak height. Plotting the data against a quantity proportional to $E/W(E) \equiv E^{1-0.66}$ is seen to display the photo-peaks with constant width

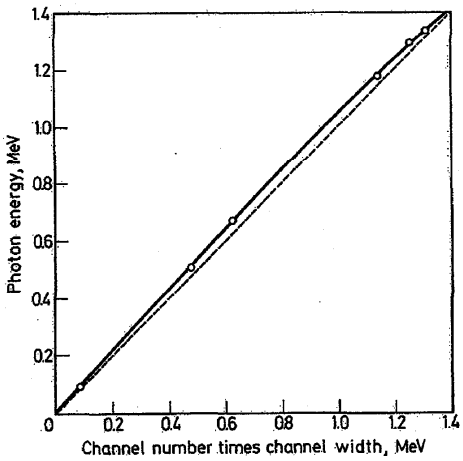

Fig. 3. Relationship between pulse height and photon energy. Points – experimental calibration data; solid line – least-squares fit to points, expressed by $E = -0.0009 + 1.1016\,h - 0.0676\,h^2$, where h is the product, channel width times channel number, in MeV; dashed straight line of unit slope is included for comparison

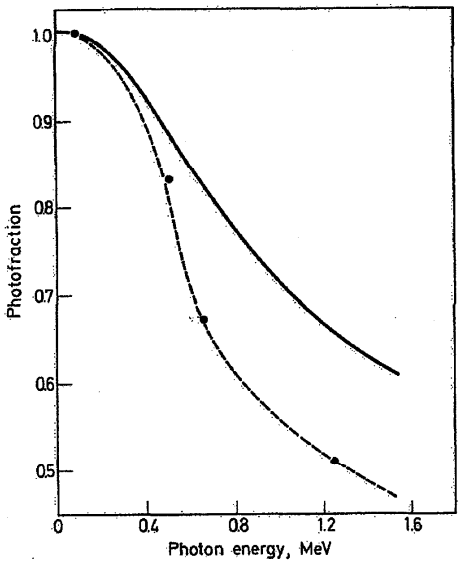

Fig. 4. Comparison of experimental and theoretical photofractions. Solid line – theory, plane-parallel beam of 3.8-cm diameter, incident perpendicularly on a 10.2-cm x 12.5-cm diameter crystal; dashed line – approximate fit to experimental data (filled circles)

Detector Resolution Function: Pulse-height distributions were measured for the four calibration sources. The experimental photopeaks were fitted with Gaussian curves chosen so as to reproduce the observed full width at half maximum, $W(E)$. As shown in Figure 2, a good fit was obtained with (a) an energy dependence of $W(E)$ of the form $W(E) \propto E^{0.66}$, which is similar to that reported for other NaI(Tl) detectors [10], and (b) a resolution for the ^{137}Cs line of $W(0.661)/0.661 = 11.0$ percent. Figure 3 shows the relationship between photon energy and pulse height obtained from the calibration data. The points mark the locations of the peaks of the fitted Gaussian curves. The solid line represents a second-degree polynomial fit to within 1 percent of the experimental points.

Influence of Detector Scattering on Experimental Response Function: The difference between the response functions computed for the bare detector and the pulse-height distributions measured for the calibration sources can be illustrated by a comparison of the theoretical and experimental photofractions, as shown in Figure 4. Differences of this type have been reported before in the literature [1]. In Figure 4, the difference – as expected – is seen to be larger for the higher photon energies, for which interactions with matter in the vicinity of the detector are more likely to result in an increase in the Compton continuum. In the present experimental geometry, the Compton continuum of the measured ^{60}Co pulse-height distribution actually was about 80 percent larger than that computed for the bare detector. However, in the subtraction process applied here to isolate the scatter present in the incident radiation beam (see Section 3.2), the local scatter contribution tends to cancel. This is the case because all the measured incident spectra are dominated by the 1.17-MeV and 1.33-MeV lines of ^{60}Co, with less than 20 percent of incident scatter components the local scatter contribution due to matter in the vicinity of the detector therefore is nearly identical in all of them.

3.2. *Unfolding Procedure and Isolation of Scatter Spectra*

The photon-energy spectra are obtained from the measured pulse-height distributions by solving Eq. (1). Since the methods employed for solving this equation are treated in detail in the literature (for a review, see, e.g., the papers by Trombka et al. [7–9]), only the most salient features applicable to the present work are discussed in this section.

Transformation to Finite Matrix Equation and Choice of Energy Intervals: In practice, to solve the integral Eq. (1) it is first transformed into a set of linear matrix equations

$$H_i \cong \sum_j R_{ij} T_j, \tag{3}$$

H_i and T_j representing the elements of the experimental pulse-height distribution and of the unfolded spectrum, with i designating the pulse-height channel number and j the energy-interval number for the response matrix with elements R_{ij}.

It has been shown previously [8] for functions similar to the present theoretical response functions, that the spacing of the basis elements, R_{ij}, in the matrix should not be greater than one-half of the full width at half maximum, $W(E)$, of the photopeak if there

is to be no loss of information in the transformation from an integral equation to a matrix equation. However, an adequate reproduction of pulse height spectra can be achieved with separations of 0.75 $W(E)$. In addition to reducing the size of the required response matrix and, hence, the computational effort, these larger separations help to damp out oscillations near high-intensity lines in the photon spectrum. The basis set used for the present study included response functions at E_0 = 1.33 MeV and 1.17 MeV, at an energy midway between the two, and twenty-seven others at midpoints of energy intervals $\Delta E_j \approx 0.75\ W(E)$, extending the coverage down to 0.055 MeV. The values for the matrix elements, R_{ij}, for these intervals were obtained from the initial thirteen theoretical functions by cubic-spline interpolation [11].

Matrix Solution: The experimental pulse-height distributions were obtained with 200 analyzer channels, while 30 energy intervals were considered appropriate in the unfolding. After corrections for electronic gain and zero shifts*, this set of 200 linear equations in 30 unknowns (T_j) was solved by the technique of weighted linear least squares and matrix inversion developed by Trombka, et al. [7–9]. This technique yields a measure for the goodness of fit between the composite spectrum, made up of the elements of the response-function matrix, and the pulse-height distribution to be unfolded (the so-called "reduced χ^2 value").

Isolating the Scatter Spectra: The spectra of the scattered photons stemming from the source, the source housing, and the collimating system, were obtained by subtracting the common component from any two of the unfolded total incident spectra, after normalization at 1.33 MeV. Let $n_j^{(1)}$ and $n_j^{(2)}$ be the number of photons in the jth interval for the incident spectra (1) and (2), characterized by the total number of incident photons,

$$N^{(1)} = \sum_j n_j^{(1)} \quad \text{and} \quad N^{(2)} = \sum_j n_j^{(2)}.$$

Then the difference in the scatter contributions of the two spectra in the jth interval, Δs_j, may be written as $n_j^{(2)} - \alpha n_j^{(1)}$, where $\alpha \equiv [n_j^{(2)}/n_j^{(1)}]_{1.33\ \text{MeV}}$.

Assessing the Uncertainties in Unfolding and Subtraction Procedures: The main sources of uncertainty in the determination of the spectral elements, T_j, are (a) the reduced χ^2 value of the unfolding process and (b) the uncertainty originating from the statistical fluctuations in the counting rate, which may be denoted by σ^2. The errors shown in Figures 6 through 10 and in Table 2 represent the product, $\sigma\chi$, in each interval j, as propagated through the summation, subtraction, and division processes required in the isolation of the scatter spectra. The uncertainties in the theoretical response functions are estimated to be much smaller than those due to unfolding and subtraction.

* Virtually no gain shift was required, and the correction for zero shift was never larger than one-half channel. Factors for these corrections were determined by the best weighted least-squares fit of the theoretical response functions at 1.33 MeV to the corresponding photo-peaks in each experimental pulse-height distribution.

Table 1. Collimator Settings Used. Distance, face of source to beam-defining edge of collimator: ~44 cm. The field sizes listed for a distance of 80 cm are those referred to in the paper as "nominal field sizes"

Approximate jaw openings (cm^2)	Field sizes (cm^2) for source-to-detector distance		
	80 cm	108 cm	204 cm
13.8 x 13.8	25 x 25	33.8 x 33.8	63.8 x 63.8
11.1 x 11.1	20 x 20	27.0 x 27.0	51.0 x 51.0
8.6 x 8.6	15 x 15	20.3 x 20.3	38.3 x 38.3
6.0 x 6.0	10 x 10	13.5 x 13.5	25.5 x 25.5
3.4 x 3.4	5 x 5	6.8 x 6.8	12.8 x 12.8
3.4 x 13.8	5 x 25	6.8 x 33.8	12.8 x 63.8

4. Experimental Results

4.1. Pulse-Height Distributions

Pulse-height distributions were obtained with the simulation source both free in air and in the source housing. Table 1 gives approximate dimensions for the six jaw openings used in the experiment. In the second column

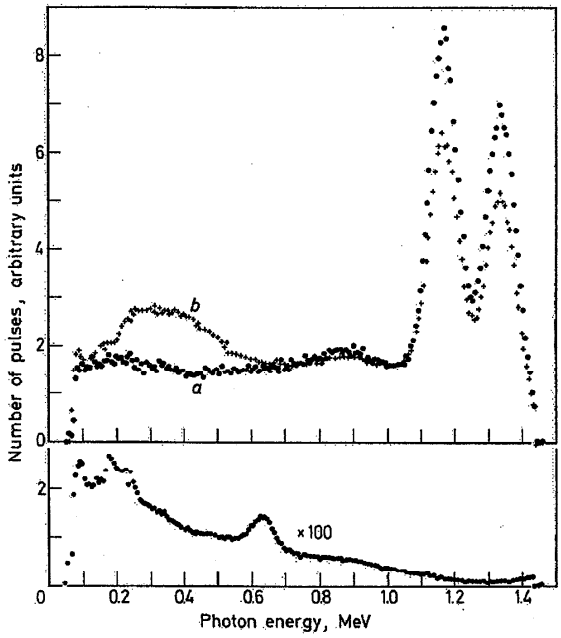

Fig. 5. Typical experimental pulse-height distributions. Top: Superimposed distribution of scatter-free source (a), and of simulation source in source housing, with largest collimator opening (b), for approximately equal numbers of events recorded in the detector. Bottom: Background spectrum, with ordinates 100x those of (b)

Table 2. Number of scattered photons in 0.05-MeV intervals, for different collimator settings. The values are expressed in percent of the total number of incident photons of energies between 0.1 and 1.33 MeV. Distance: ~1 meter

ΔE MeV	Total scatter contribution in energy interval ΔE (percent of total number of incident photons) for nominal field sizes						
	5 x 5 cm^2	8 x 8 cm^2 *	10 x 10 cm^2	15 x 15 cm^2	20 x 20 cm^2	25 x 25 cm^2	5 x 25 cm^2
0.10–0.15	0.37	0.40	0.42	0.42	0.43	0.51	0.36
0.15–0.20	0.60	0.63	0.66	0.65	0.67	0.69	0.58
0.20–0.25	1.22	1.20	1.19	1.19	1.17	1.28	1.13
0.25–0.30	1.62	1.67	1.71	1.69	1.71	1.74	1.62
0.30–0.35	1.58	1.68	1.78	1.75	1.78	1.78	1.67
0.35–0.40	1.48	1.67	1.85	1.85	1.87	1.87	1.71
0.40–0.45	1.39	1.63	1.86	1.85	1.87	1.88	1.63
0.45–0.50	1.17	1.40	1.61	1.61	1.63	1.64	1.40
0.50–0.55	0.88	1.06	1.23	1.26	1.27	1.28	1.08
0.55–0.60	0.62	0.75	0.87	0.91	0.92	0.94	0.78
0.60–0.65	0.47	0.57	0.67	0.70	0.71	0.75	0.59
0.65–0.70	0.41	0.51	0.60	0.62	0.64	0.69	0.50
0.70–0.75	0.36	0.46	0.55	0.57	0.60	0.65	0.45
0.75–0.80	0.28	0.37	0.46	0.49	0.53	0.58	0.39
0.80–0.85	0.20	0.31	0.41	0.45	0.50	0.56	0.33
0.85–0.90	0.14	0.29	0.42	0.45	0.51	0.62	0.27
0.90–0.95	0.10	0.28	0.45	0.48	0.55	0.71	0.23
0.95–1.00	0.09	0.30	0.49	0.50	0.58	0.79	0.21
1.00–1.17	0.74	1.60	2.42	1.06	1.72	3.38	0.11
1.17–1.33	0.37	0.81	1.21	0.53	0.86	1.69	0.06
$\sum_{0.1}^{1\ \mathrm{MeV}}$	13.0 ± 2.0	15.2 ± 2.0	17.2 ± 1.9	17.4 ± 1.8	17.9 ± 1.7	19.0 ± 1.7	14.9 ± 1.8

* Interpolated; setting corresponds to a 10 x 10 cm^2 field at a distance of 1 meter.

are the resulting field sizes at a source-to-detector distances of 80 cm. These field sizes are referred to as "nominal field sizes" throughout this paper, and are used to identify the particular collimator settings. The corresponding approximate field sizes at the distances actually used (108 cm and 204 cm) are listed in the last two columns.

Typical background-corrected pulse-height distributions obtained at a distance of about 1 meter are shown in Figure 5, for (a) the scatterfree source and (b) the simulation source inside the source housing. Shown also is the spectrum of the relatively insignificant background. The small peak in the background spectrum in the vicinity of 0.66 MeV probably stems from natural radioactivity in the building concrete rather than from ^{137}Cs.

4.2. *Spectra of Scattered Photons*

As outlined in Section 3.2, the number of scattered photons in the jth interval, $\Delta s_j \equiv n_j^{(1)} - \alpha n_j^{(2)}$ was obtained from the two spectra to be compared. The values plotted in the ordinates of Figures 6 through 10 are percent scatter per unit energy, $100\,\Delta s_j/(N^{(2)}\Delta E_j)$, where by definition, $N^{(2)} > N^{(1)}$.

Total Scatter Contribution: The number spectrum of the scattered photons due to the combined effect of source, housing, and collimator in Figure 6, where $(100\Delta s_j)/N^{(2)}\Delta E_j$ is plotted for the simulator source in place inside the housing at a distance of about 1 meter from the detector. The spectrum substracted was that of the essentially scatter-free source, suspended in air, also at a distance of about 1 meter from the detector. The resulting total-scatter spectra are shown for a number of different collimator settings, with the nominal field-size designations given in Table 1 for the 80-cm source-to-detector distance. The unfolded data actually are histograms. The points in the figure are plotted at the center of the histogram intervals, both for ease of presentation and to facilitate curve fitting. The error bars give the uncertainty in the unfolding procedure as discussed in Section 3. Below 1 MeV, the data are represented by a smooth curve, obtained by a weighted least-squares cubic-spline fit of the points [12]. Above 1 MeV, where the unfolded data oscillate badly, no fit was attempted. Rather, a step function was drawn with a total area equal to that under the unfolded data, such that the areas under the steps at $1 < E \leqslant 1.17$ MeV and $1.17 < E \leqslant 1.33$ MeV were in the ratio of 2 to 1.* Also shown are the values of

* The ratio of 2 to 1 is an approximation, reflecting the knowledge that the two equal-intensity lines both contribute to the Compton continuum below 1.17 MeV, while only the 1.33-MeV line contributes above this energy.

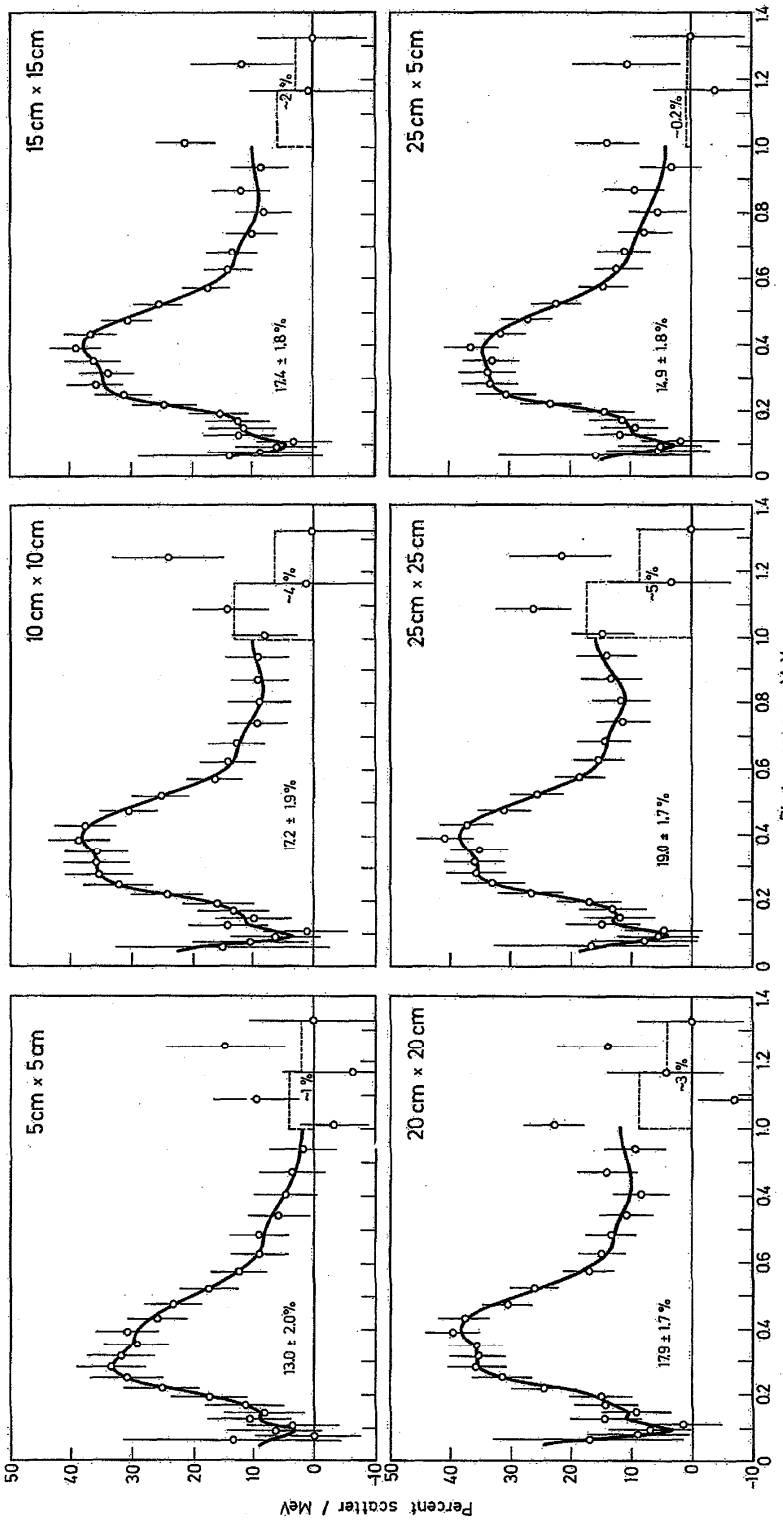

Fig. 6. Total scatter contribution obtained as difference between total spectrum of simulation source in head, with nominal field sizes indicated, and spectrum of scatter-free source. Source-to-detector distance: ~ 1 meter

the integrated scatter contribution, in percent of the total number of photons in the simulation spectrum below and above 1 MeV, as derived from the fitted data. The errors indicated for the data below 1 MeV were compounded in quadrature from the unfolding errors of the two initial spectra. The energies of the photons forming the bulk of the total scatter contribution are seen to lie between about 0.2 and 0.6 MeV, with peaks at about 0.28 and 0.44 MeV. The rise in the number of photons per energy interval toward the low-energy limit of detectability may be an artifact caused by an incomplete subtraction of the lead K x-ray peak originating in the detector collimator. Noticeable also is a small peak between 0.10 and 0.15 MeV, which may be observed in the results of earlier investigators as well (see, e.g., Cormack and Johns [13]). This peak evidently occurs only in the spectrum of the ^{60}Co beams containing appreciable scatter components (note that in Figure 5 it is absent from the pulse-height distribution of the scatter-free beam), and thus does not disappear in the subtraction process. It is likely to be not an attribute of the incident beam, but rather to be backscatter by the photomultiplier of, variously, the

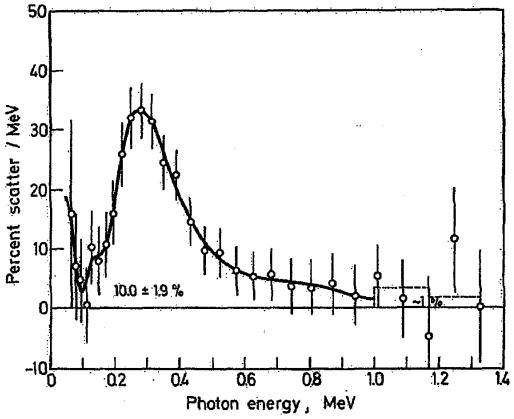

Fig. 7. Scatter contribution of simulation source proper

0.28- and 0.44-MeV components of the incident beam, resulting in 0.13- and 0.16-MeV scattering peaks. This effect was not accounted for in the theoretical response

Table 3. Number of scattered photons in 0.05-MeV intervals, contributed by housing and collimator and by source proper. The values are expressed in percent of the total number of incident photons of energies between 0.1 and 1.33 MeV. Distance: ~1 meter

	Total scatter contribution in energy interval ΔE (percent of total number of incident photons)						
	From housing and collimator for nominal field sizes			From difference for pairs of nominal field size*			
ΔE MeV	5 x 5 cm^2	10 x 10 cm^2	25 x 25 cm^2	25 x 25 cm^2 minus 5 x 5 cm^2	10 x 10 cm^2 minus 5 x 5 cm^2	25 x 25 cm^2 minus 10 x 10 cm^2	Simulation Source Proper
0.10–0.15	0.08	0.15	0.25	0.18	0.08	0.10	0.31
0.15–0.20	0.05	0.16	0.20	0.16	0.10	0.05	0.56
0.20–0.25	0.01	0.07	0.23	0.20	0.05	0.15	1.24
0.25–0.30	0.03	0.23	0.32	0.29	0.21	0.10	1.65
0.30–0.35	0.13	0.44	0.50	0.38	0.33	0.08	1.51
0.35–0.40	0.36	0.83	0.89	0.57	0.49	0.10	1.16
0.40–0.45	0.60	1.14	1.18	0.65	0.58	0.09	0.82
0.45–0.50	0.62	1.11	1.16	0.61	0.53	0.09	0.55
0.50–0.55	0.49	0.87	0.94	0.50	0.42	0.10	0.41
0.55–0.60	0.32	0.60	0.68	0.39	0.30	0.11	0.32
0.60–0.65	0.21	0.43	0.52	0.33	0.24	0.11	0.27
0.65–0.70	0.17	0.39	0.48	0.33	0.22	0.11	0.24
0.70–0.75	0.14	0.35	0.45	0.33	0.22	0.12	0.22
0.75–0.80	0.09	0.29	0.42	0.34	0.21	0.14	0.21
0.80–0.85	0.04	0.26	0.43	0.40	0.23	0.18	0.18
0.85–0.90	0.00	0.29	0.50	0.49	0.29	0.22	0.14
0.90–0.95	−0.03	0.34	0.59	0.60	0.36	0.26	0.10
0.95–1.00	−0.04	0.39	0.65	0.67	0.40	0.28	0.08
1.00–1.17	0.10	1.83	2.81	2.63	1.75	0.95	0.66
1.17–1.33	0.05	0.92	1.41	1.32	0.87	0.47	0.33
$\sum_{0.1}^{1\ \text{MeV}}$	3.3 ± 1.6	8.3 ± 1.5	10.4 ± 1.3	7.4 ± 1.7	5.3 ± 1.8	2.3 ± 1.8	10.0 ± 1.9

* Percentage referred to total number of photons in the spectrum with the larger scatter contribution.

functions, so that these peaks are allowed to remain in the unfolded spectra.

To aid in the further use of the data presented in Figure 6, the number of scattered photons in successive 0.05-MeV intervals, obtained by integrating the fitted curves numerically, is given in Table 2. The questionable results below 0.1 MeV have been disregarded. The percentages of photons above 1 MeV are given in two entries, corresponding to the step-function representation discussed above. The origin of the major peaks shown in Figure 6 becomes evident if one compares the spectrum of the simulation source proper with that emerging from the housing used with varying degrees of collimation. A discussion of the origin of these peaks is given in the following sections.

Scatter Spectrum of the Simulation Source: The scatter spectrum of the simulation source proper is shown in Figure 7, where the values of $100\Delta s_j/(N^{(2)}\Delta E_j)$ are plotted for the simulation source suspended in air at a distance of about 1 meter from the detector. Again, the spectrum subtracted is that of the essentially scatterfree source, suspended in air at about the same distance from the detector. Numerical data derived from the fitted curve of the scatter components in successive 0.05-MeV intervals are shown in the last column of Table 3. The spectrum has only one major peak, coinciding with that of the 0.28-MeV peak of the total scatter spectrum (Fig. 6). The scatter contribution below 1 MeV is about 10 percent, which is about one-half of the total scatter for the beam obtained with the source in the housing with the widest collimator setting and about three-fourths of the total scatter obtained with the smallest collimator setting. In view of the fact that one is dealing here with a source that was especially designed for low scatter, this seems quite large. Data on the influence of source geometry on the scatter contribution are being evaluated at present.

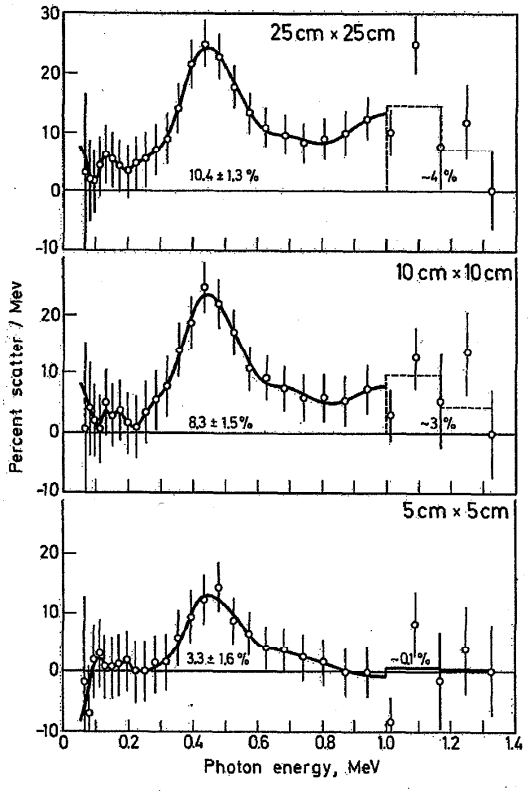

Fig. 8. Scatter contribution of housing only, for three representative nominal field sizes; distance ~1 meter from source

Scatter Contribution of Housing: Figure 8 shows scatter spectra due to the housing, including the collimator, for three representative collimator settings. The corresponding integrated values for successive 0.05-MeV intervals are given in columns 2 to 4 of Table 3. These spectra were obtained from the difference between the total spectra emerging from the housing at a distance of about 1 meter and the spectrum of the simulation source suspended in air at the same distance. The major peak at about 0.44 MeV now appears isolated. It is seen to decrease materially as the collimator aperture is decreased, an effect that also can be observed in the series of graphs of Figure 6. This peak thus clearly is attributable to scatter by the housing.

Shielding by Source Collimator: The extent to which one may be able to decrease the scatter contribution by reducing aperture size is shown in Figures 9 and 10. In Figure 9, the number of scattered photons integrated over the energy range from 0.1 to 1 MeV and expressed in percent of the total number of incident photons is plotted for a series of collimator settings. Data are included for distances of both 1 and 2 meters from the source. While the integral scatter contribution is seen to lower by about 5 percent for the 2-meter distance (where the decrease amounts to almost one-half of the total scatter for the 5-cm x 5-cm nominal field size at a

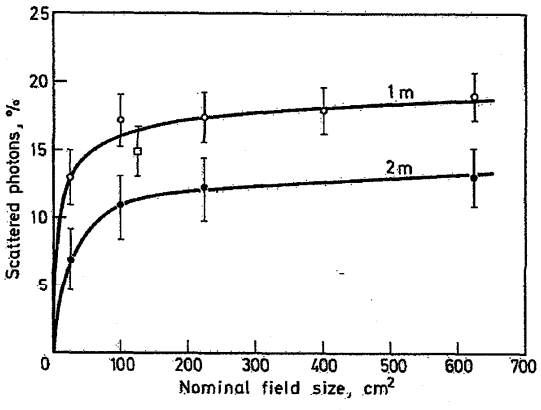

Fig. 9. Scatter contribution for different nominal field sizes and distances of ~1 m and ~2 m. The circles indicate data for square fields; the square is for a nominal 5-cm x 25-cm field size

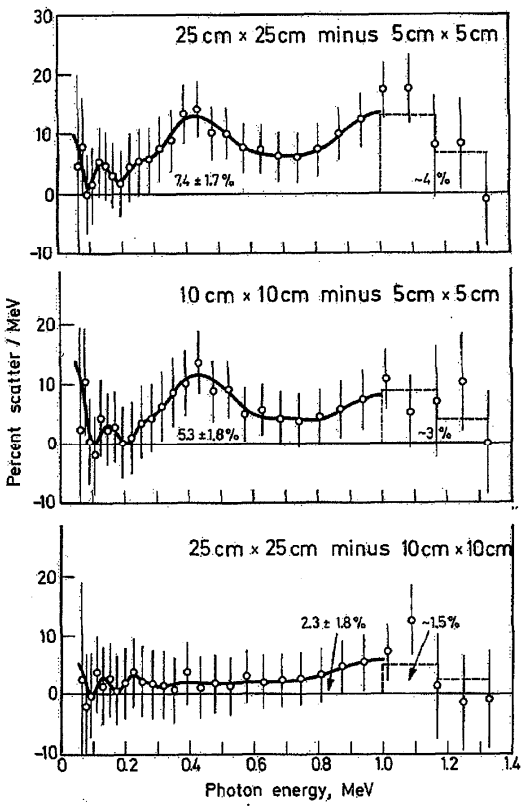

Fig. 10. Difference between scatter contributions of spectral pairs of different nominal field sizes; distance: ~1 meter from source

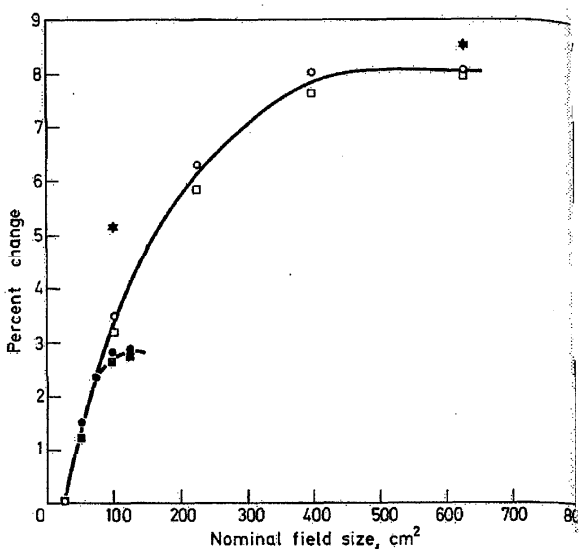

Fig. 11. Increase in exposure with nominal field size. Points obtained from ionization measurements with source-to-detector distance of ~1 meter (circles) and ~2 meters (squares); open symbols – square fields; filled symbols – rectangles with two sides of 5 cm length; stars – square fields computed from spectral distributions of Figure 10

distance of 1 meter) the trend with nominal field size is about the same. The important parameter is the collimator aperture, which determines the extent to which the collimator absorbs the scatter produced inside the source housing. For both distances, the total scatter contribution rises by about 4 percent as nominal field size is increased from 5 cm x 5 cm to 10 cm x 10 cm. A further increase to a nominal field size of 25 cm x 25 cm produces an additional increment of only 2 percent. It is interesting to note that the scatter contribution for the rectangular field does not differ significantly from that of a square field of the same area.

Examples for the difference between the spectral distributions of the scatter emerging from some of the different apertures are shown in Figure 10. An increase in the aperture beyond the 10 cm x 10 cm setting, while further increasing the overall scatter, is seen not to increase any further the relative contribution to the 0.44-MeV peak. Above 1 MeV, in spite of the poor quality of the unfolded data, a definite trend toward an increase in the scatter contribution with increasing square aperture can be seen, reaching about 4 percent for the 25 cm x 25 cm setting at a distance of 1 meter The corresponding numerical values are shown in columns 5–7 of Table 3.

4.3. Scatter Contribution in Terms of Exposure

Of practical interest is the scatter contribution to the exposure measured in terms of ionization in air. Figure 11 shows for the two distances from the source, the increase in exposure with collimator-aperture size. As pointed out in Section 4.2, the important parameter again is collimator aperature, distance and field shape being of only minor influence. In view of the findings of others [14], it may be of interest to note that we too observe that the output becomes essentially constant for nominal field sizes beyond 20 cm x 20 cm. Plotted also in Figure 11 for two collimator settings and a distance of ~1 m, is the change in exposure computed from the corresponding number spectra of Fig. 10 by weighting the values in each interval with the average energy and energy-absorption coefficient of air for the particular interval.

5. Overall Uncertainty in Scatter Determination

Among the independent sources for uncertainties in the determination of the scatter spectra are limitations in the linearity and stability of the analyzer electronics, uncertainties due to photon scattering in the detector system, uncertainties entering into the calculation of the response-function matrix, and uncertainties connected with the unfolding procedure which also include the statistical error in the counting rate.

The analyzer system was checked for deviations from linearity. None was detected for the counting rates and total counts used in the experiment. As discussed in Section 3.1, uncertainties unrelated to the unfolding

process tend to cancel in the subtractions and divisions involved in isolating the scatter spectra. Therefore, we consider the error bars shown in the figures to be representative of the total uncertainty in the determination of the scatter contribution between 0.1 and 1 MeV. A useful error analysis for the experimental data in the region between 1.00 and 1.33 MeV is not feasible since the experimental data are too erratic there. Results of experiments and calculations [1–6] indicate that the scatter contribution below 0.1 MeV is negligible.

6. Comparison with the Results of Other Authors

A meaningful comparison with the results of other investigators is difficult because of differences in source, housing, and source-collimator geometries, as listed in Table 4. However, the broad features of the spectra can be compared: The scatter from the encapsulated source itself shows a considerable contribution above ~0.2 MeV with the exact location of the peak varying with capsule, sleeve, and backing materials (i.e., spacer, plug, etc), and a tendency toward somewhat higher energies in the case of high-Z materials. There is a wide variation in the total scatter contribution with source, source-housing, and collimator geometry. A contribution of scattered photons below 1 MeV of at most 2 percent of the total number was reported for the Saclay primary reference-standard assembly [6]. The source assembly of the Bureau International des Poids et Mesures, as simulated by Costrell, showed a photon-intensity contribution of about 7 percent below 0.8 MeV [1]. The scatter contribution in the NBS facility is comparable to those reported by Costrell [1] and by Aitken and Henry [2] for realistic therapy-type facilities, with the number of scattered photons below 1 MeV varying between 13 and 19 percent of the total number of photons. The therapy-type facilities studied by Guiho et al. [6] were reported to have considerably larger scatter contributions, varying between about 30 and 37 percent depending on the type of the source housing.

Table 4. Comparison of Source Geometries

Investigator	Source geometry
Costrell [1]	pellets in all-steel capsule (teletherapy-type geometry)
	discs either bare or in steel capsule with W plug, separated from discs by air-space (BIPM-type source)
Scrimger and Cormack [3]	discs in steel capsule with W sleeve
Aitken and Henry [2]	pellets in all-steel capsule
Goodwin [4]	teletherapy-type geometry
Guiho et al. [6]	discs or pellets in steel capsule, enclosed in W capsule; W sleeve (teletherapy-type geometry)
	French primary Standard, Saclay
Present study	single layer of pellets in steel capsule, W plug in contact with pellets (teletherapy-type geometry)

Acknowledgment: The authors are indebted to M. J. Berger of the Radiation Theory Section of the NBS Center for Radiation Research for helpful discussions, and to P. J. Lamperti of the Dosimetry Section for carrying out the exposure measurements. M. Ehrlich is especially grateful to C. E. Dick of the X-Ray Section for his guidance in various stages of the work.

References

1. Costrell, L.: Health Physics *8*, 261 (1962)
2. Aitken, J.H., Henry, W.H.: Internat. J. Appl. Rad. and Isotopes *15*, 713 (1964)
3. Scrimger, J.W., Cormack, D.V.: Brit. J. Radiol. *36*, 514 (1963)
4. Goodwin, P.N.: Radiology *87*, 205 (1966)
5. Appendix B, ICRU Report 18, Specification of High Activity Gamma-Ray Sources. International Commission on Radiation Units and Measurements. Washington, D.C. (1970)
6. Guiho, J.P., Legrand, J., Grinberg, B.: Dosimetry in Agriculture, Industry, Biology and Medicine. IAEA Proceedings Series, Vienna (1973)
7. Trombka, J.I., Schmadebeck, R.L.: Nuclear Instr. Methods *62*, 253 (1968)
8. Trombka, J.I., Senftel, F., Schmadebeck, R.L.: Nuclear Instr. Methods *87*, 37 (1970)
9. Reedy, R.C., Arnold, J.R., Trombka, J.I.: J. Geophys. Res. *78*, 5847 (1973)
10. Berger, M.J., Seltzer, S.M.: Nuclear Instr. Methods *104*, 317 (1972)
11. See, e.g., Ahlberg, J.H., Nilson, E.N., Walsh, J.L.: Theory of Splines and their Applications, Chapter II. New York: Academic Press, 1967
12. Thompson, R.F.: NASA Goddard Space Flight Center Publication X-693-73-321 (1973)
13. Cormack, D.V., Johns, H.E.: Brit. J. Radiol. *31*, 497 (1958)
14. Switzer, D.W.: Quarterly Bull, A.A.P.M. Qtr. Bull. *7*, 107 (1973)